Investigation of in vivo beam range verification in carbon ion therapy using the Doppler Shift Effect of prompt gamma: A Monte Carlo simulation study

Yang Han[a], Xiaobin Tang[a,b,*], Changran Geng[a], Diyun Shu[a], Chunhui Gong[a,c], Xudong Zhang[a], Shaojuan Wu[a], Xinxin Zhang[a]

[a] Nanjing University of Aeronautics and Astronautics, Department of Nuclear Science and Engineering, 29 Yudao St., Nanjing, 210016, China
[b] Collaborative Innovation Center of Radiation Medicine of Jiangsu Higher Education Institutions, 29 Yudao St., Nanjing, 210016, China
[c] National Institute of Nuclear Physics (INFN), Section of Pavia, Pavia, Italy

ABSTRACT

Carbon ion therapy has received increasing attention because of its excellent physical dose distribution and high biological effect comparing against the conventional radiotherapy. However, the range uncertainty is still a major issue that limits further improvement of the treatment efficiency. Hence, we propose a novel method for reducing the range uncertainty in carbon ion therapy based on the Doppler Shift Effect of prompt gamma (PG), which can quantify the average carbon energy by the significant energy shift of the 4.44 MeV PG in the spectrum and then calibrate the range. Specifically, the influences of heterogeneity, initial carbon beam configuration, and detected direction are thoroughly discussed using the Monte Carlo simulation in this paper. Results show a moderate difference (< 3.5%) between the Monte Carlo simulation and the analytical calculation, which verify the theoretical feasibility and veracity of the proposed method. The different initial energies (200, 225, 250, 300, and 400 MeV/u) and energy spreads (0%, 0.5%, 1%, 2%) of carbon beam have a not obvious influence on the accuracy of this method. When the detected direction changes from 90° to 50°, the PG energy shift overturns from "red shift" to "blue shift" and the difference value increases significantly. Moreover, for inhomogeneous phantoms, this method can distinguish the different ranges with blocks filled by different materials (bone, adipose, and air) in the beam path. Finally, through the analysis of range verification error with cavities of different thicknesses (0–30 mm) in the water phantom, the precision of the proposed method in theory is determined to be 0.008%–6.253%, and this value can be less than 3% with an appropriate detection site. These results indicate that the measurement of the PG energy shift could be applied to reduce the range uncertainty on the basis of the Doppler Shift Effect in carbon ion therapy.

1. Introduction

Charged-particle therapy has recently been paid more attention for its unique interaction and energy deposition pattern (Geng et al., 2015; Loeffler and Durante, 2013; Schulz-Ertner et al., 2006). Carbon ion radiotherapy, one of the charged-particle therapies, has been given importance because of its biological effectiveness (Lin et al., 2017b; Tsujii and Kamada, 2012). It can kill radio-resistant cancer cells availably, and therefore reduce the probability of tumor recurrence. However, the range uncertainty of the radiation beam seriously affects the efficiency of carbon ion therapy, which is similar to the other charged-particle therapies (e.g. proton therapy). This uncertainty originates from the positioning error, CT image resolution, CT value to stopping power conversion factor error, anatomical change and the complex biological effectiveness (Paganetti, 2012). In clinical practice, the planner usually extends the treatment volume by the range margin to cover the whole tumor in the robustness manner, which increases the integral dose to the normal tissue and reduces the superiority of carbon ion therapy. Various quantitative range margins from 2.5% + 1.5 mm to 3.5% + 3 mm for proton therapy (Paganetti, 2012) and 5 mm (Tsujii et al., 2014) or 3.5% + 2 mm for carbon ion therapy have been applied by different therapeutic centers and organizations to account for the range uncertainty. These margins could potentially be narrowed if in-vivo range monitoring is achieved the range verification.

Various techniques to measure the beam range for charged-particle therapy have been developed, most of which rely on the emission of
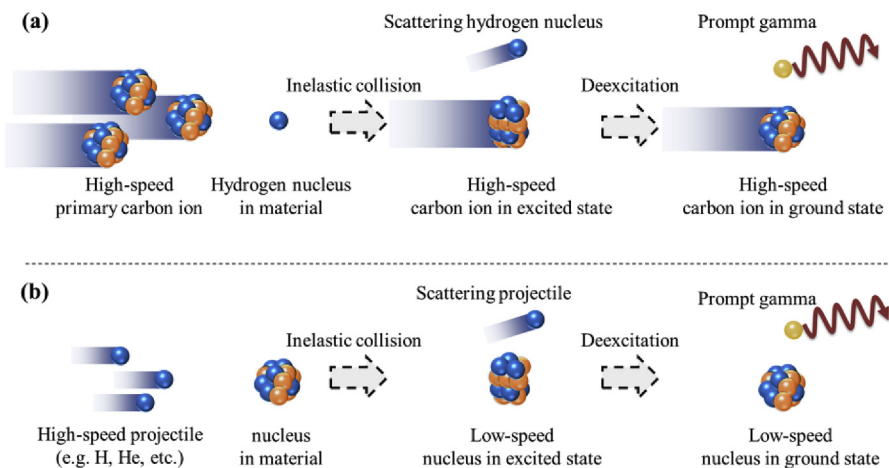

Fig. 1. (a) Schematic diagram of the shifted PG generated from the high-speed carbon ion in excited state after the collision between the primary carbon ion and the hydrogen nucleus; (b) Schematic diagram of the characteristic PG generated from the low speed residual nucleus after the collision between high-speed projectile and target nucleus in material.

secondary charged particle, delayed gamma and prompt gamma (Knopf and Lomax, 2013). Secondary charged particles generated from the nuclear collision which have a longer range than the primary particles, can be used to determine the range of the primary particles non-invasively (Finck et al., 2017; Traini et al., 2017). Positron emission tomography (PET) is a delayed gamma measurement technology for range verification by detecting the coincident gamma from annihilate, which relies on the distribution of the positron emitting isotopes (e.g. ^{11}C, ^{15}O, ^{13}N, ^{30}P and ^{38}K) generated from the nuclear interaction (Enghardt et al., 2004; Ferrero et al., 2018; Min et al., 2013). The main limitation of PET imaging for range verification is the washout effect, that is, the location of gamma emission does not fully coincide with that of the nuclear interaction occurring because of the off-line detection mode and long decayed time (Moteabbed et al., 2011). By contrast, prompt gamma (PG) detection during the charged-particle treatment can be used for real-time range verification (Krimmer et al., 2018; Xie et al., 2017). PG is originated from the de-excitation of the excited nucleus produced in the nuclear interaction. Various PG detection systems have been designed. The slit collimator detection system, which is consisted of a single slit collimator and scintillator array, have achieved one-dimensional PG detection in clinical proton therapy (Priegnitz et al., 2015). Also, the array-type detection system containing scintillator array and collimator array is the another choice (Lin et al., 2017a; Min et al., 2012), but the resolution is limited by the thickness of collimator considering the penetration of MeV PG. Moreover, Compton camera has been designed to detect PG profile in charged-particle therapy (Aldawood et al., 2017; Ortega et al., 2015). Nevertheless, since the profile of the PG yield is not in good agreement with the Bragg peak because of the different physical mechanisms of energy deposition and PG generation, these relative methods are difficult to achieve a quantitative range accurately. Selecting an appropriate PG energy window and removing the influence of secondary neutron by the time-of-flight technology could improve the agreement between gamma profile and the Bragg peak in relative detection systems (Biegun et al., 2012; Golnik et al., 2014; Verburg et al., 2012). Verburg et al. proposed an absolute detection system composed of a slit collimator and a primary scintillator to measure the water equivalent depth and C/O concentration with the knowledge of PG emission cross section by gamma spectroscopy (Hueso-González et al., 2018; Verburg and Seco, 2014). However, this method is difficult to apply for carbon ion therapy because of the influence of multiple nuclear fragments which make the PG emission cross section complicated.

In this paper, we propose a novel range verification method based on the Doppler Shift Effect of prompt gamma in carbon ion therapy which is different from the existing methods in this field. In carbon ion therapy, high-speed nuclear fragments (i.e. projectiles) with an excited state can be generated by nucleus-nucleus reaction (Kraan, 2015). The

excited carbon nucleus is one of the most common projectiles. Because of the Relative Doppler Effect (Huang and Lu, 2004), prompt gammas (de-excitation within 10^{-16} s) from the projectiles can be shifted from its original energy (e.g. 4.44 MeV for carbon nucleus) with a certain observe direction. By quantifying the PG energy shift, we can measure and verify the carbon range. Specifically, the influences of heterogeneity, initial carbon beam configuration, and detected direction will be thoroughly discussed using the Monte Carlo simulation to verify the feasibility of the proposed technology.

2. Principle and methods

2.1. Principle

Along with the primary carbon ions through the human body, complex reaction can occur between ion and electron or nucleus in the material. Interaction with electron allows the carbon ion loss its energy along the beam path continuously. Interaction with nucleus causes the nuclear reaction and produces residual nuclei. Here, we call those residual nuclei at low speed or even in static in the lab frame the residual target nuclei (e.g. the high-mass residual nucleus from the collision between the secondary proton and material nucleus). Those residual nuclei at high speed can be defined the residual projectiles (e.g. high-speed second neutron, proton, heavy ion) (Kraan, 2015). Some residual projectiles (including the carbon nuclei) can be excited and undergo de-excitation within 10^{-16} s. In our research, we found that the carbon nuclei (^{12}C) can be excited after inelastic collision with the hydrogen nuclei in material. According to the law of momentum conservation, these carbon ions can reach an excited state with slightly deflected travel direction, and then de-excite to the ground state with PG emission on-the-fly as shown in Fig. 1-a. This interaction can be regarded as the opposite process that much lighter projectile collides with the carbon nucleus in material and then PG emits from the low-speed carbon nucleus (i.e. excited target nucleus) as shown in Fig. 1-b. We have to consider the Lorentz boost for those PG generated from the high-speed excited carbon nuclei, which leads to the Doppler Shift Effect.

In the center-of-mass frame, the maximum possible energy of PG emitted from the excited carbon ion is 4.44 MeV (Fig. 2-a). However, for the high-speed carbon nuclei (e.g. the speed of the 400 MeV/u carbon ion is nearly 0.7 times of the speed of light in vacuum), the energy of the emitted PG deviates from 4.44 MeV in a certain emission direction because of the Doppler Shift Effect. This phenomenon should be consistent with the Doppler shift law as follows (Gill, 1965):

$$f' = f \cdot \frac{\sqrt{1-\beta^2}}{1-\beta \cdot cos\theta},$$
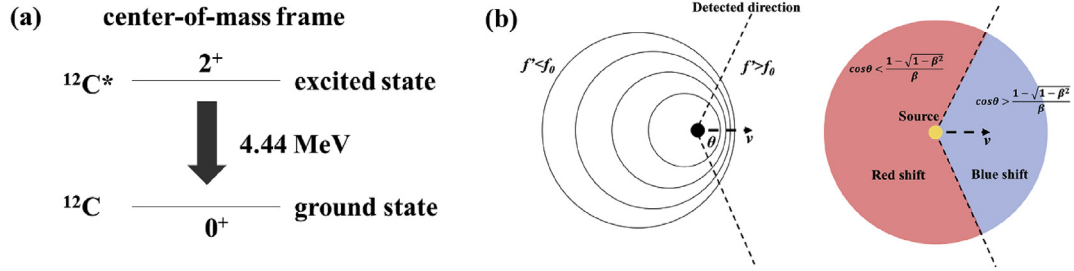
(1)

Fig. 2. (a) The de-excitation of carbon nucleus in the center-of-mass frame; (b) Diagram of red shift and blue shift caused by the Doppler Shift Effect. (For interpretation of the references to colour in this figure legend, the reader is referred to the Web version of this article.)

where f' is the frequency of the electromagnetic wave after the Doppler shift, f is the original frequency of the electromagnetic wave without the Doppler shift, β is the ratio of the speed of carbon ion and the speed of light in vacuum, and θ is the angle between the detection line and the flight direction of carbon ion. According to Eq. (1), a blue shift (PG energy > 4.44 MeV) can occur when $cos\theta > \frac{1-\sqrt{1-\beta^2}}{\beta}$, while a red shift (PG energy < 4.44 MeV) should be observed when $cos\theta < \frac{1-\sqrt{1-\beta^2}}{\beta}$ (Fig. 2-b).

2.2. Mathematical model and analytical calculation method

We construct a mathematical model to elucidate the relationship between the energy shift and the carbon energy along the beam path by combining the special theory of relativity (Resnick, 1971) and Eq. (1). The shifted PG energy (E'_γ) can be determined by the equation as follows:

$$E'_\gamma = E_\gamma \cdot \frac{\frac{m_0 c^2}{m_0 c^2 + E_c}}{1 - cos\theta \cdot \sqrt{1 - \left(\frac{m_0 c^2}{m_0 c^2 + E_c}\right)^2}}, \tag{2}$$

$$\text{or } E_C = \left[\frac{cos^2\theta \cdot E'^2_\gamma + E^2_\gamma}{E'_\gamma \cdot \left(E_\gamma \pm cos\theta \cdot \sqrt{E^2_\gamma - sin^2\theta \cdot E'^2_\gamma}\right)} - 1\right] \cdot m_0 c^2, \tag{3}$$

where m_0 is the carbon ion rest mass, c is the light speed in vacuum, and E_c is the kinetic energy of carbon ion.

The material characteristics along the beam path should be used to determine the carbon energy at a certain depth according to the Bethe formula as follows (Bethe, 1953):

$$-\left(\frac{dE}{dx}\right) = \frac{4\pi}{m_e c^2} \cdot \frac{n z^2}{\beta^2} \cdot \left(\frac{e^2}{4\pi\varepsilon_0}\right)^2 \cdot \left[\ln\left(\frac{2 m_e c^2 \beta^2}{I \cdot (1 - \beta^2)}\right) - \beta^2\right], \tag{4}$$

where $-\left(\frac{dE}{dx}\right)$ is the stopping power, m_e is the electron mass, n is the electron density, z is the charge of carbon ion, e is the amount of electron charge, I is the average ionization energy, and ε_0 is the vacuum permittivity. Through Eq. (4), average carbon ion energies can be solved along the beam path. And then, the shifted PG energy can be solved as a function of the incident depth of carbon ions (i.e. the detection site) by this analytical calculation method.

2.3. Monte Carlo method

In order to evaluate the feasibility of the proposed method and the accuracy of the mathematical model for range verification, we take the Monte Carlo simulation which have considered all the PG emission in carbon ion therapy. We use the Monte Carlo software TOPAS 3.1.2 (Perl et al., 2012), which is developed specifically for charged-particle therapy research based on Geant4.10.3.p01 (Agostinelli et al., 2003;

Allison et al., 2006, 2016), to simulate the whole particle transport process. The required physical models for this study include the "g4em-standard_opt4", "g4h-phy_QGSP_BIC_HP", "g4decay", "g4ion-binarycascade", "g4h-elastic_HP", and "g4stopping" which contain complete cross section for particle transport of the primary carbon ion and secondary particles of interest (i.e. protons, electrons, positrons, neutrons, photons, and other nuclear fragments) (Böhlen et al., 2010; Lechner et al., 2010).
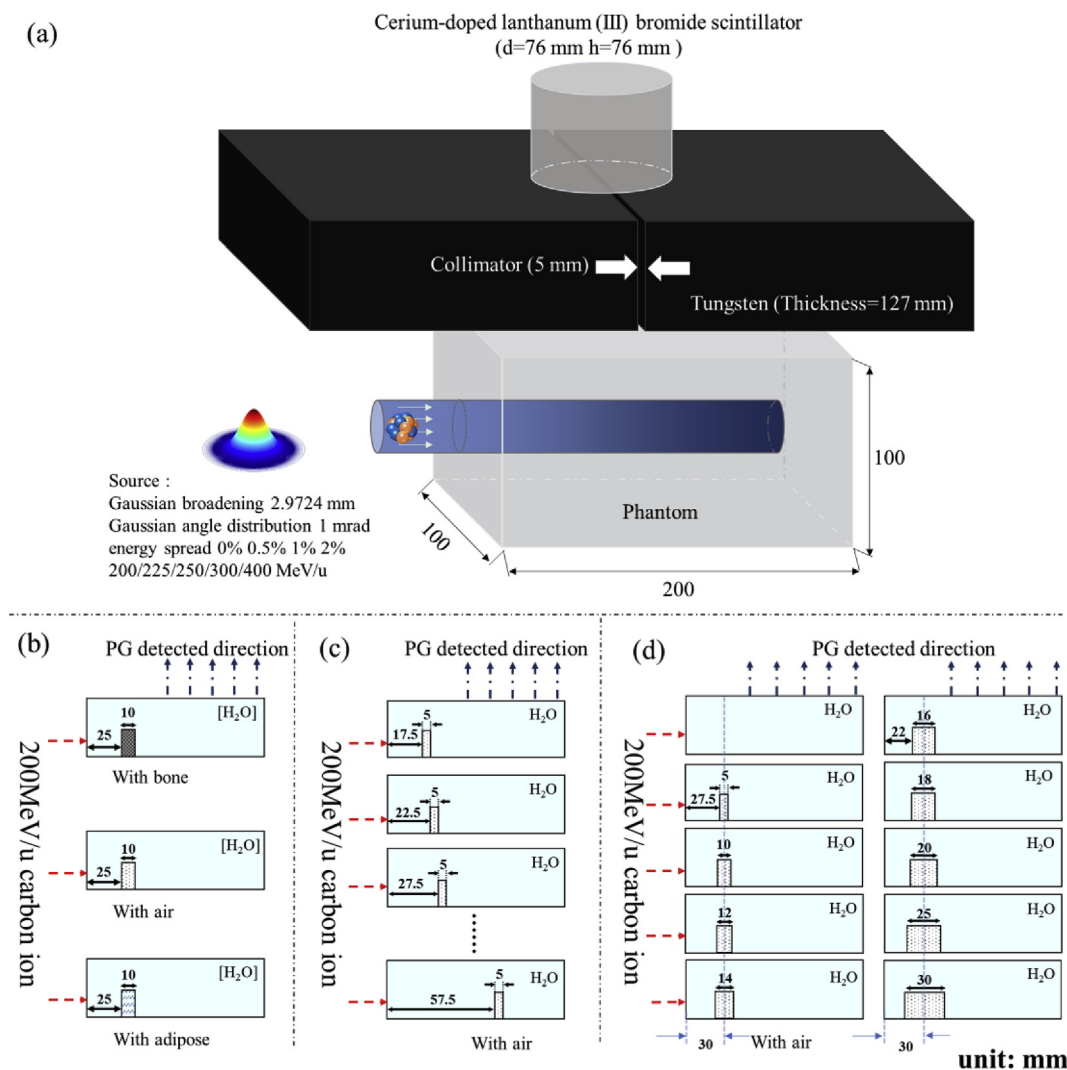
The geometry of Monte Carlo simulation is constructed as shown in Fig. 3-a. Carbon ion beams with different initial energies and spreads (i.e. pencil beam with 2.9724 mm Gaussian broaden, 1 mrad Gaussian angle distribution, five beam energies: 200, 225, 250, 300, and 400 MeV/u, four energy spreads: 0%, 0.5%, 1%, 2%) are used to irradiate the $100 \times 100 \times 200$ mm³ water phantom. A tungsten collimator on the side of the phantom with a thickness of 127 mm and the slit opening of 5 mm is set on the side of the phantom. A cerium-doped lanthanum (III) bromide scintillator detector with the length and diameter of 76 mm is placed after the collimator slit. The detected direction is set as 90° (Fig. 3-a) and 50°, respectively. To study the influence of tissue heterogeneity on the method, three heterogeneous conditions (see Fig. 3-b, 3-c and 3-d) have been studied. As shown in Fig. 3-b, 10 mm thick blocks made of three different materials (i.e. bone, air, and adipose) are set at the depth of 30 mm in the water phantoms. In Fig. 3-c, there is an air cavity with a constant thickness value of 5 mm in the different depths (i.e. 25, 30, 35, 40, 45, 50, 55, 60 mm) in each phantom. The other phantoms are with an air cavity of different thicknesses (i.e. 0, 5, 10, 12, 14, 16 18, 20, 25, 30 mm) at the same depth of 30 mm (see Fig. 3-d).

For ensuring satisfied statistical uncertainty (< 0.2% in average), 5×10^8 primary carbon ions are simulated to achieve the PG spectrum detection. A two-step simulation method is adopted to improve the computational efficiency. First, we score the detail information of generated gamma rays as a phase space data file in phantom. In this step, the secondary gamma does not continue to be transported, and the delayed gamma is removed by a neutron filter, which means we do not score gamma whose ancestor is neutron. Neutron filter can partially realize the time-of-flight method in practice. Second, starting from the gamma ray, which is stored in the phase space file, the gamma ray will be continuously transported in the phantom and to the detection system. The detected PG data are recorded on the scintillator surface. We have not fully simulated the process of the scintillation detector as that is not the main focus of the current manuscript, and it will be discussed in the following studies. The shifted PG energy is quantified from the PG spectrum by Gaussian fitting and linearly rejecting method to remove the background.

3. Results and discussion

3.1. PG energy spectra in different detection depth

The PG energy spectra measured at depths of 16.3 cm and 14.8 cm with a detected direction of 90° when the water phantom is irradiated

Fig. 3. (a) Schematic diagram of the geometric model for Monte Carlo simulation; (b) Water phantoms with 10 mm block of different materials (i.e. bone, air, and adipose) at the depth of 30 mm; (c) Water phantoms with an air cavity of same thicknesses (5 mm) at the different depths (i.e. 25, 30, 35, 40, 45, 50, 55, 60 mm); (d) Water phantoms with an air cavity of different thicknesses (i.e. 0, 5, 10, 12, 14, 16 18, 20, 25, 30 mm) at the depth of 30 mm.

by the 300 MeV/u carbon beam using the TOPAS simulation are shown in the Fig. 4. There are five observable PG peaks in each graph (four characteristic PG peaks: 2.31 MeV from ^{14}N*, 4.44 MeV from ^{12}C*, 5.27 MeV from ^{15}O*, 6.18 MeV from ^{16}O*, and one red-shifted PG peak from the 4.44 MeV PG). These characteristic PGs are mostly from the residual target nucleus with an excited state, so these PGs maintain at its original energy without the significant Doppler Shift Effect due to the low speed (or static) of the target nucleus. As can be observed, there is Doppler Broadening Effect for these characteristic PGs because of the thermal motion. In fact, the Doppler Burdening Effect can be regard as the multiple superposition of Doppler Shift Effect, because the thermal motion is disordered and multidirectional. However, a significant Doppler Shift Effect requires projectiles moving in one direction with a high speed. In this paper, we proposed that the Doppler shift effect of the specific 4.44 MeV (from high-speed ^{12}C* de-excitation) can be used for the Carbon energy estimation. Quantifying every peaks in the PG energy spectrum (Fig. 4-b), we obtain that the yield ratio of the red-shifted PG to the 2.31 MeV PG is 1:1.031, the yield ratio of the red-shifted PG to the 4.44 MeV PG is 1:1.468, the yield ratio of the red-shifted PG to the 5.27 MeV PG is 1:0.907, and the yield ratio of the red-shifted PG to the 6.18 MeV PG is 1:0.942. Of course, these ratios changes under different conditions (i.e. detection depth, incidence carbon energy). However, it can be known that the yield of red-shifted

peak is comparable to other characteristic PG peaks, so the Doppler Shift Effect can be detected and quantified using a proper detection system (e.g. the energy- and time-resolved PG detector) (Verburg et al., 2013). The red-shifted peak in Fig. 4a and b differs in energy because of the different mean carbon kinetic energies in the two detection sites, which can lead to the different energy shift according to the relationship between carbon kinetic energy and Doppler shift.

There are some inconspicuous peaks whose energies are less than 2.31 MeV from the de-excitation of ^{15}O*, ^{11}C*, ^{15}N*, ^{11}B*, ^{10}B*. Because the yields of these characteristic PG are relatively low, these PG peaks can be changed by the background signal more easily, even be submerged. ^{11}C*, ^{11}B* and ^{10}B* can have a high kinetic energy (i.e. these nuclei may be projectiles), which can lead to the Doppler Shift Effect, but the yield is relatively small (Gunzert-Marx et al., 2008). Also, ^{15}O* and ^{15}N* are almost at low speed. So, the Doppler Shift Effect is not the main reason leading to the energy change of these peaks in Fig. 4 a and b. As we did not propose the method with the whole spectrum but specifically on the 4.44 MeV PG, this will not affect the conclusion.
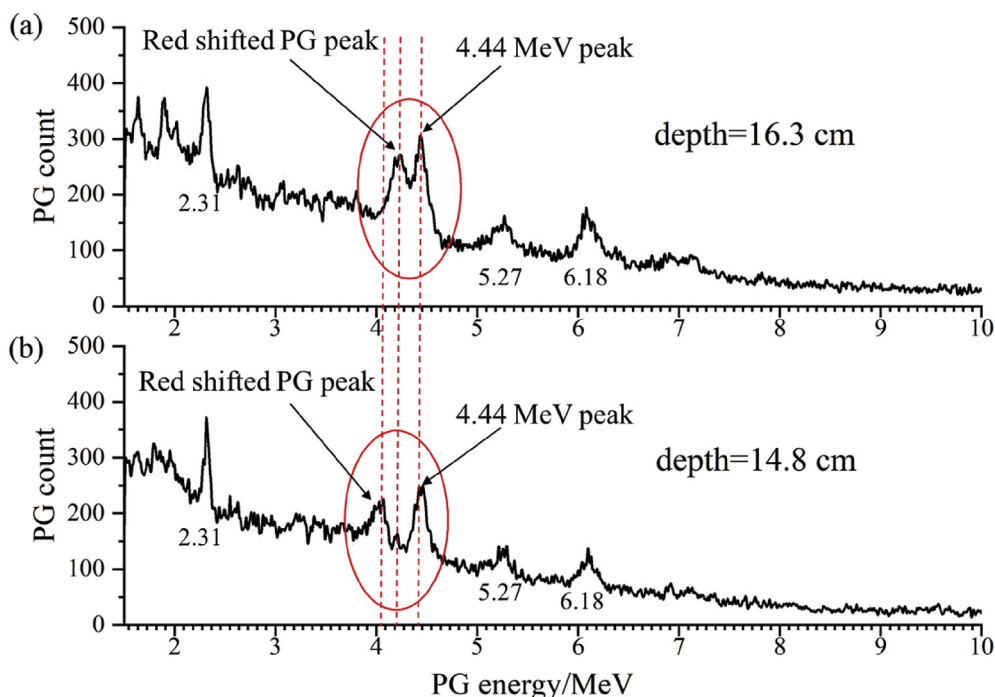
Fig. 4. PG energy spectra on the detector with a detected direction of 90° at the depths of 16.3 cm (a) and 14.8 cm (b) when the water phantom is irradiated by the 300 MeV/u carbon beam.
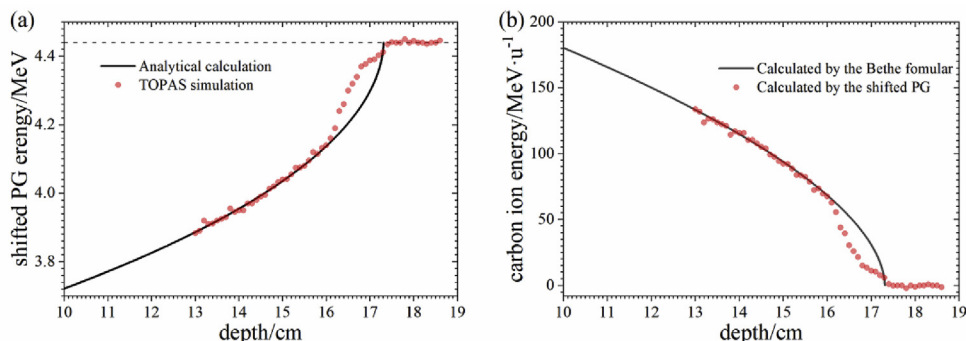

Fig. 5. (a) The shifted PG energy along the beam path from analytical calculation (black line) and TOPAS simulation (red point) when the 300 MeV/u carbon beam irradiates the water phantom; (b) The average carbon ion energy along the beam path calculated by the Bethe formula (black line) and the shifted PG (red point) when the 300 MeV/u carbon beam irradiates the water phantom. (For interpretation of the references to colour in this figure legend, the reader is referred to the Web version of this article.)

Table 1
Difference values between the results from analytical calculation and TOPAS simulation with various beam energies.

Beam size	Energy (MeV/u)	Difference value			
		> 1.5 cm[a]	< 1.5 cm[b]	all regions	maximum
Gauss broadening	200	0.297%	1.558%	0.832%	2.565%
2.9724 mm	225	0.227%	1.943%	0.813%	3.483%
Gauss angle	250	0.364%	1.737%	0.833%	2.592%
distribution	300	0.116%	1.513%	0.560%	2.708%
1 mrad	400	0.171%	1.154%	0.630%	2.356%
Pencil beam					
(mono energy)					

[a] Outside 1.5 cm ahead of the range (without peak overlap).
[b] Within 1.5 cm ahead of the range (with peak overlap).

3.2. Profile of the shifted PG energy and average carbon energy in homogeneous water phantom

The shifted PG energies with detected direction set to 90° have been determined when the 300 MeV/u carbon beam irradiates the water phantom (Fig. 5-a). According to the analytical calculation, the inequation for red shift ($cos\theta < \frac{1-\sqrt{1-\beta^2}}{\beta}$) has always been consistent whatever the value of β, when we set θ to 90°, that means the shifted PG energy always keep less than 4.44 MeV along the primary beam path. Comparing the analytical calculation (black line) and TOPAS simulation (red point), we find their results have similar variations and the average absolute difference value along the beam path is determined to 0.56% in this condition. However, when the detection site is at the depth of approximately 16–17 cm, the TOPAS simulation results are generally higher than the analytical calculation because of the energy straggling and the overlapping peak phenomenon as shown in Fig. 4-a. The overlapping peak phenomenon means that when the kinetic energy of carbon ion is relatively low near the end of the range, the shifted peak will be close to the 4.44 MeV peak leading to the systematic uncertainty in determining the energy of the shifted PG peak. We also compare the average carbon ion energy calculated by the Bethe formula and the shifted PG along the beam path. According to the results shown in Fig. 5-b, 75 MeV/u could be a preliminary critical value for the mathematical model (see section 2.2) to describe the relationship accurately. Moreover, as we can achieve the reconstruction of the average energy of the carbon beam based on the proposed method, this may be used in the experiments in other fields where the carbon energy needs to be measured non-invasively.
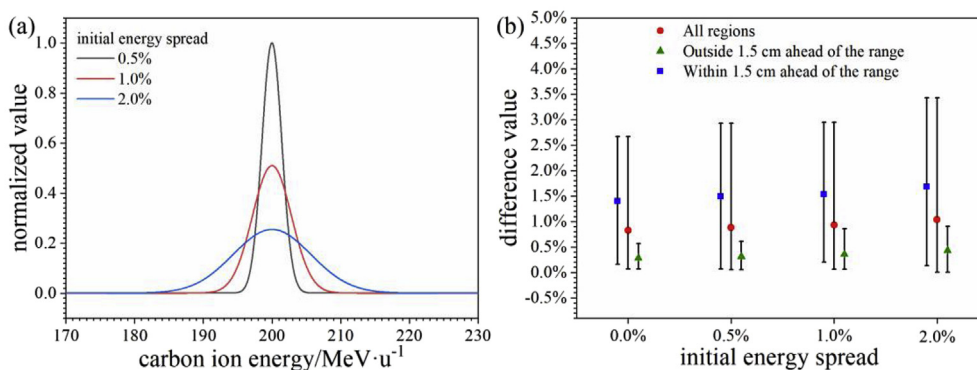
Fig. 6. (a) Different energy distributions of initial carbon ion with various energy spreads (0%, 0.5%, 1%, 2%); (b) The difference values with the various initial energy spreads. The bars show the maximum and minimum difference values.
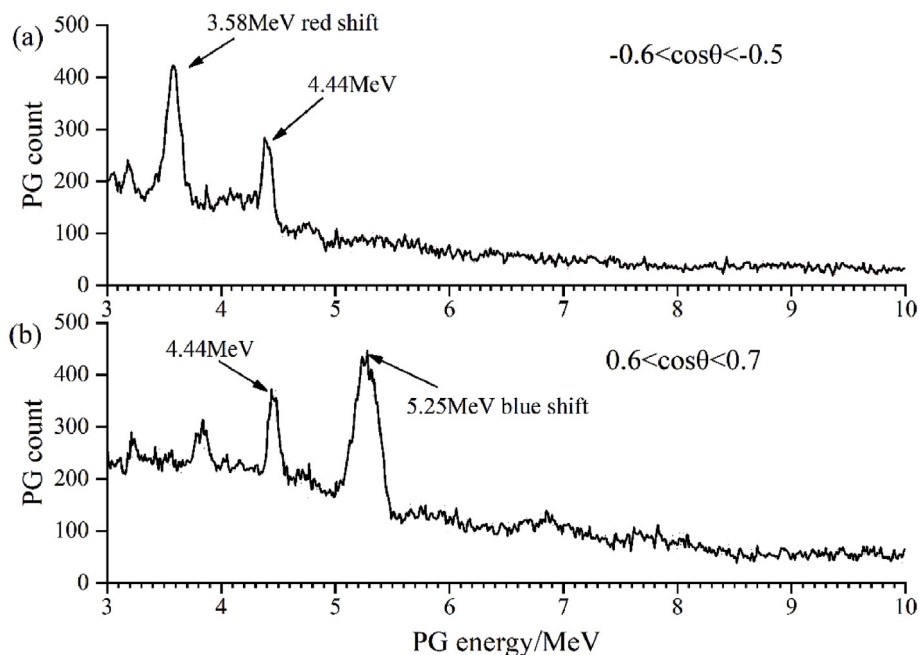

Fig. 7. PG ray production spectra with the emission angles of $-0.6 < \cos\theta < -0.5$ and $0.6 < \cos\theta < 0.7$ at the depth of 7.8 cm in the polyethylene phantom irradiated by the 200 MeV/u carbon beam.

3.3. Different beam configurations

In clinical carbon ion therapy, carbon beams with various energies are used to cover the tumor target with spot scanning technology. Therefore, we set different conditions to discuss whether these beam configurations can influence the effectiveness of the proposed method. The influences caused by the different initial carbon energies are shown in Table 1. The impact is relatively weak as all the total difference values are less than 1%. Such a tiny difference value means a good coincidence between the TOPAS simulation and analytical calculation. However, the difference value is relatively large in the "> 1.5 cm" group (i.e. outside 1.5 cm ahead of the range) comparing to the "< 1.5 cm" group (within 1.5 cm ahead of the range). The result indicates that the overlapping peak phenomenon can seriously influence the accuracy of this method with the current mathematical model. The maximum difference value, which exists in the "< 1.5 cm" group, is determined to be less than 3.5%.

Fig. 6 shows the influence of initial energy spread to the accuracy of the proposed method. There is a slightly larger total and maximum difference value when we set a larger initial energy spread. It is the evidence that the energy straggling is the one of the reasons which make the poor agreement near the under of the range (see Fig. 5-a). But,

because of the different cross sections of PG generation with different carbon energies, the influences of energy straggling far from the Bragg peak and near the Bragg peak are different in theory.

3.4. Different detected directions

From Eq. (1) in section 2.2, we can solve the relationship between the detected direction and the PG energy shift in theory. As the red shift phenomenon of PG has been verified when the detected direction is set to 90°, whether an appropriate energy shift will occur when the detected direction changes is discussed in this section. The result can indicate whether the proposed method can be performed from other directions to improve the accuracy. We select polyethylene as the phantom material, because it has no characteristic gamma energy higher than 4.44 MeV, which will affect the results potentially. Fig. 7 shows the PG production spectra when the gamma emission angle is set to $-0.6 < \cos\theta < -0.5$ and $0.6 < \cos\theta < 0.7$. A significant red shift is noted in Fig. 7-a, while a blue shift is observed in Fig. 7-b, which is consistent to the analytical prediction.

Fig. 8 shows the shifted PG energy along the beam path obtained from TOPAS simulation and the analytical calculation when the collimator slit is set to 50°. Through analytical calculation, we can find the
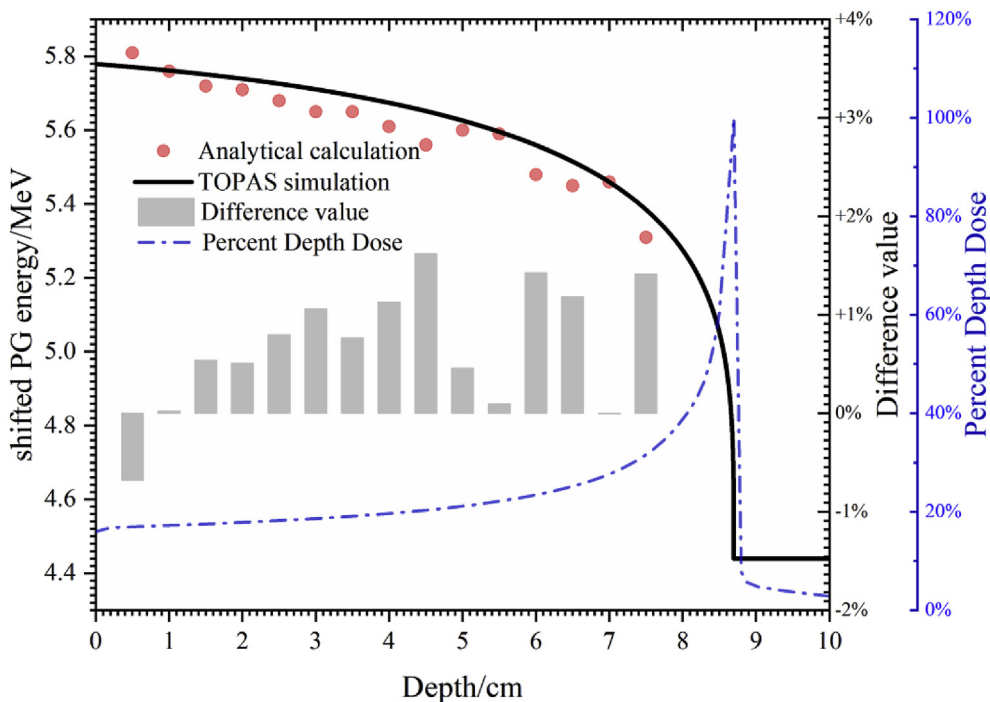
Fig. 8. The shifted PG energy along the beam path from analytical calculation (black line) and TOPAS simulation (red point) when the carbon beam energy is 200 MeV/u and the detected direction is 50°. (For interpretation of the references to colour in this figure legend, the reader is referred to the Web version of this article.)
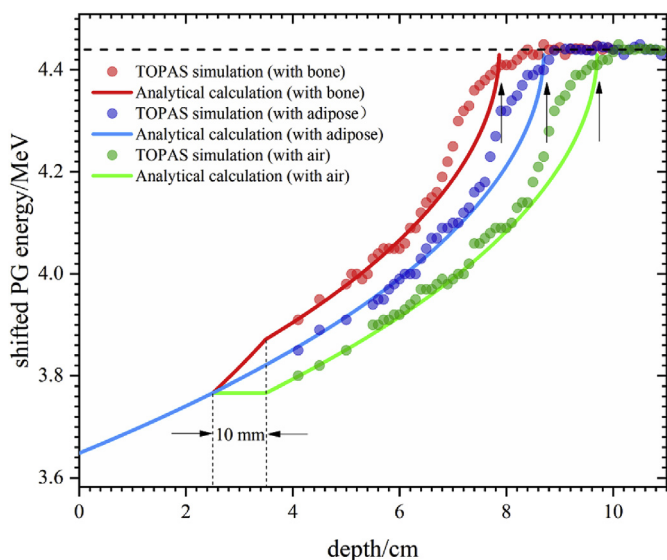

Fig. 9. The shifted PG energy along the beam path from analytical calculation (solid line) and TOPAS simulation (point) with three blocks made of different material (bone/adipose/air) in the water phantom.

Table 2
Difference values between the results from analytical calculation and TOPAS simulation in three different inhomogeneous situations.

Material	Difference value			
	> 1.5 cm[a]	< 1.5 cm[b]	all regions	maximum
H_2O + 10 mm bone	0.255%	1.752%	0.786%	2.502%
H_2O + 10 mm adipose	0.364%	2.162%	0.913%	3.093%
H_2O + 10 mm air	0.268%	1.392%	0.730%	3.055%

[a] Outside 1.5 cm ahead of the range (without peak overlap).
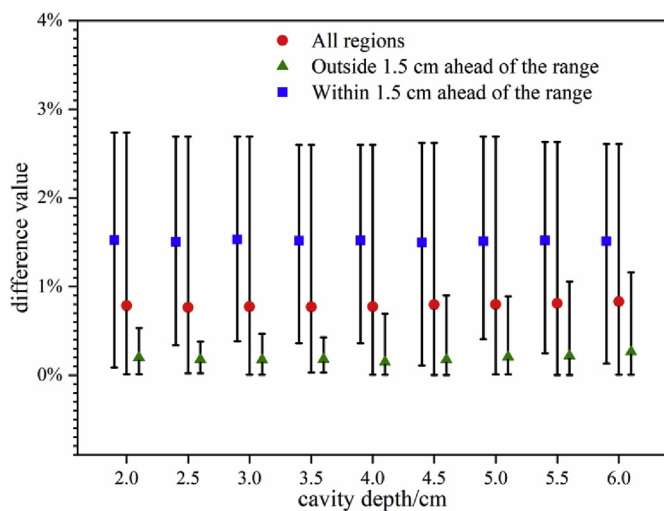[b] Within 1.5 cm ahead of the range (with peak overlap).

Fig. 10. The difference values between analytical calculation and TOPAS simulation results with a cavity (0.5 cm thickness) in the different depths in the beam path. The bars show the maximum and minimum difference values.

inequation for blue shift (i.e. $cos\theta > \frac{1 - \sqrt{1 - \beta^2}}{\beta}$) has always been consistent when we set θ to 50° and the initial carbon beam energy to 200 MeV/u. The overall trends of the TOPAS simulation and the analytical calculation results are almost the same, but there is a relatively larger difference value compared to the case of 90°. This phenomenon may be caused by the more serious carbon energy broadening when the detected direction is slanted to the beam incident direction.

3.5. PG energy shift for heterogeneous phantoms

Considering the complex geometrical heterogeneity in the human body, we construct the Monte Carlo simulation geometry model to approximate the heterogeneity condition (see Fig. 3-b). The analytical calculation (solid line) and the Monte Carlo simulation results (point)
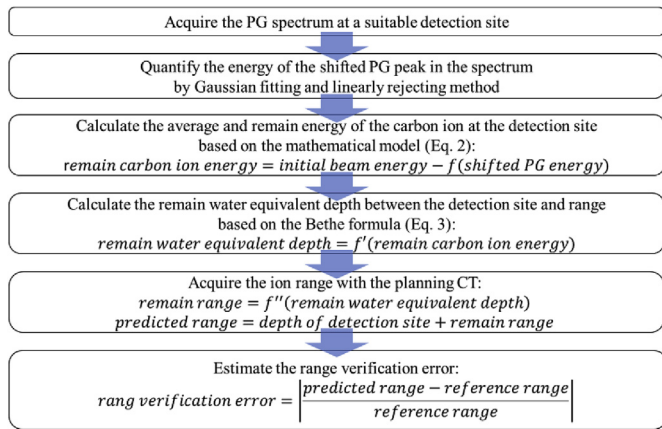
Fig. 11. Flow diagram for range verification.

Table 3

Range verification error between the predicted range using the proposed method and the reference range with various detection sites and cavity thicknesses in the water phantom irradiated by 200 MeV/u carbon beam.

Material	Range verification error					
	6.5 cm	7.0 cm	7.5 cm	8.0 cm	8.5 cm	9 cm
H_2O	0.478%	0.210%	1.140%	6.253%	2.218%	–
H_2O + 0.5 cm air	0.103%	0.452%	0.199%	0.210%	6.250%	2.097%
H_2O + 1.0 cm air	1.249%	1.249%	1.931%	0.088%	2.624%	5.940%
H_2O + 1.2 cm air	0.374%	0.638%	0.482%	0.195%	0.530%	1.575%
H_2O + 1.4 cm air	0.967%	0.085%	1.084%	0.291%	0.211%	0.008%
H_2O + 1.6 cm air	0.075%	0.612%	0.322%	0.508%	0.171%	0.359%
H_2O + 1.8 cm air	0.587%	0.022%	0.351%	0.295%	0.221%	0.254%
H_2O + 2.0 cm air	0.437%	0.525%	0.243%	0.089%	0.388%	0.171%
H_2O + 2.5 cm air	1.750%	1.137%	0.501%	0.232%	0.085%	0.371%
H_2O + 3.0 cm air	0.358%	0.269%	1.747%	0.480%	1.393%	0.956%

are shown in Fig. 9. The red, blue, and green data are obtained with bone, adipose, and air blocks in the water phantom, respectively. The results indicate that this range verification method could well distinguish these three heterogeneous conditions considering that the TOPAS simulated values are in good agreement with the predicted values by the analytical calculation. The quantitative difference values are shown in Table 2. The total average difference value is less than 1% and the maximum difference value is approximate 3%.

Fig. 10 shows the little influence of difference value when we set a cavity with a constant thickness value (0.5 cm) in the different depths (see Fig. 3-c). This is reasonable because of the little divergence angle (i.e. excellent current-to-flux ratio) for carbon beam.

3.6. Analysis of range verification accuracy

As we have verified the feasibility of the novel range verification method based on the Doppler Shifted Effect, a process which can be used in practice is proposed (see Fig. 11). The range verification error between the predicted range by this process and the reference range (i.e. the distal 80% point of the Bragg peak in the percent depth dose curve calculated by Monte Carlo simulation) at six detection sites and nine cavity thicknesses in the water phantom irradiated by 200 MeV/u carbon beam are shown in Table 3 and Fig. 12 (geometry is shown in Fig. 3-d). Considering the error to obtain the remaining range between the detection site and Bragg peak using the planning CT, a 0.5% error is presupposed in the fifth step as there is CT value to stopping power conversion error (Schaffner and Pedroni, 1998; Schneider et al., 1996). The results indicate that the verification error is from 0.008% to 6.253%. When the detection site is located within 1.5 cm ahead of the range, the error is large because of the overlapping peak phenomenon and energy straggling. If the detection site is chosen properly, the error for range verification can be less than 3%.
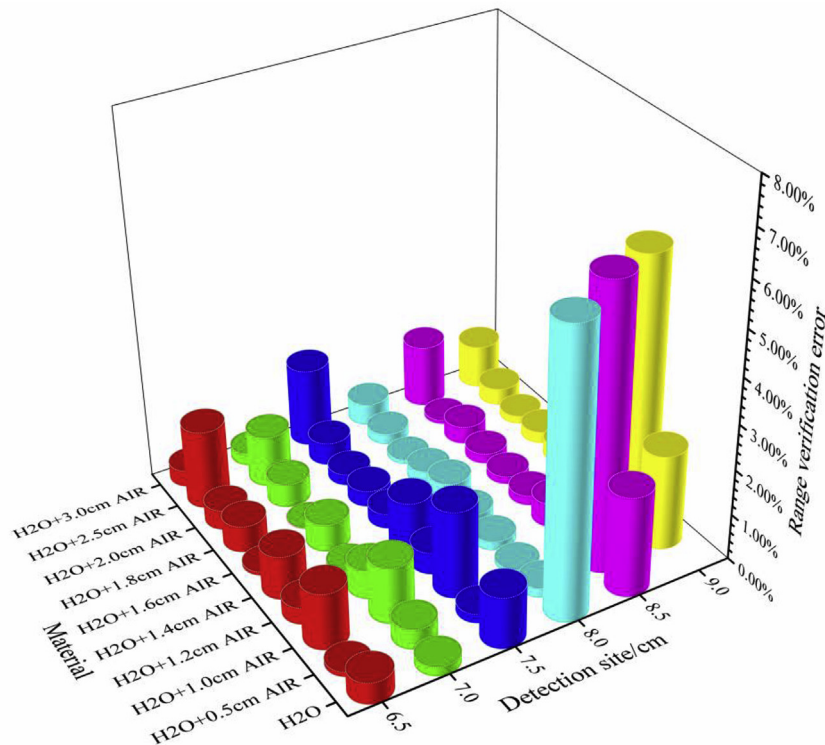

Fig. 12. Range verification error between the predicted range using the proposed method and the reference range with various detection sites and cavity thicknesses in the water phantom irradiated by 200 MeV/u carbon beam.

4. Conclusion

A system to measure the carbon ion range on the basis of the Doppler Shift Effect of PG has been proposed in this paper. A mathematical model is constructed to elucidate the relationship between the shifted PG energy and the depth of detection site in theory. Specifically, the influences of heterogeneity, initial beam configuration, and detected direction are discussed in detail. Comparison of the shifted PG energies obtained from the analytical calculation and TOPAS simulation shows that different clinically beam energies (200, 225, 250, 300, 400 MeV/u) and energy spread (0%, 0.5%, 1%, 2%) have a not obvious influence for this method with a total difference value less than 1% and a maximum value less than 3.5%. When the detected direction, which depends on the collimator slit, changes from 90° to 50°, the shifted PG overturned from the obvious red shift to blue shift and the accuracy for range verification decreases significantly. In addition, for the inhomogeneous phantom, the proposed method could distinguish different ranges at the same detection site with three different blocks (10 mm bone, adipose, and air) in the beam path. Analyzing the range error with 0 mm–30 mm cavities on the beam path shows a verification error from 0.008% to 6.253% and a possible error less than 3% with an appropriate detection site. These results indicate that the proposed method could effectively reduce the range uncertainty of the carbon ion with an appropriate detection system.

What needs to be stated is that the proposed technique is more suitable for spot scanning considering the influence of the spread-out Bragg peak in passive scattering technique. Because this work mainly focused on the preliminary theoretical feasibility and influencing factors analysis, several practical problems have not been discussed in this paper. Detailed investigation on the detection efficiency, energy resolution, multiple peak overlap and environment noise, which may hamper the identification of the energy shift peak in the spectrum, will be performed in subsequent studies. To realize future clinical applications, multi-directional detector and spectrum analysis technology based on deconvolution or machine learning can be integrated with the detection system (He et al., 2018; Liu et al., 2015), especially when the detection site is located near the end of the range. Studies on these issues are ongoing in our group and will be presented in the future. We believe that online range verification for carbon ion therapy is feasible in the future with the implementation of the proposed methodology.

Acknowledgements

References

Agostinelli, S., Allison, J., Amako, K.a., Apostolakis, J., Araujo, H., Arce, P., Asai, M., Axen, D., Banerjee, S., Barrand, G., 2003. GEANT4—a simulation toolkit. Nucl. Instrum. Methods Phys. Res. Sect. A Accel. Spectrom. Detect. Assoc. Equip. 506, 250–303.

Aldawood, S., Thirolf, P., Miani, A., Böhmer, M., Dedes, G., Gernhäuser, R., Lang, C., Liprandi, S., Maier, L., Marinšek, T., 2017. Development of a Compton camera for prompt-gamma medical imaging. Radiat. Phys. Chem. 140, 190–197.

Allison, J., Amako, K., Apostolakis, J., Araujo, H., Dubois, P.A., Asai, M., Barrand, G., Capra, R., Chauvie, S., Chytracek, R., 2006. Geant4 developments and applications. IEEE Trans. Nucl. Sci. 53, 270–278.

Allison, J., Amako, K., Apostolakis, J., Arce, P., Asai, M., Aso, T., Bagli, E., Bagulya, A., Banerjee, S., Barrand, G., 2016. Recent developments in Geant4. Nucl. Instrum. Methods Phys. Res. Sect. A Accel. Spectrom. Detect. Assoc. Equip. 835, 186–225.

Bethe, H.A., 1953. Passage of radiations through matter. Exp. Nucl. Phys. 1, 253.

Biegun, A.K., Seravalli, E., Lopes, P.C., Rinaldi, I., Pinto, M., Oxley, D.C., Dendooven, P., Verhaegen, F., Parodi, K., Crespo, P., 2012. Time-of-flight neutron rejection to improve prompt gamma imaging for proton range verification: a simulation study. Phys. Med. Biol. 57, 6429.

Böhlen, T.T., Cerutti, F., Dosanjh, M., Ferrari, A., Gudowska, I., Mairani, A., Quesada, J., 2010. Benchmarking nuclear models of FLUKA and GEANT4 for carbon ion therapy. Phys. Med. Biol. 55, 5833.

Enghardt, W., Crespo, P., Fiedler, F., Hinz, R., Parodi, K., Pawelke, J., Pönisch, F., 2004. Charged hadron tumour therapy monitoring by means of PET. Nucl. Instrum. Methods Phys. Res. Sect. A Accel. Spectrom. Detect. Assoc. Equip. 525, 284–288.

Ferrero, V., Fiorina, E., Morrocchi, M., Pennazio, F., Baroni, G., Battistoni, G., Belcari, N., Ciocca, M., Del Guerra, A., Donetti, M., 2018. Online proton therapy monitoring: clinical test of a Silicon-photodetector-based in-beam PET. Sci. Rep. 8, 4100.

Finck, C., Karakaya, Y., Reithinger, V., Rescigno, R., Baudot, J., Constanzo, J., Juliani, D., Krimmer, J., Rinaldi, I., Rousseau, M., 2017. Study for online range monitoring with the interaction vertex imaging method. Phys. Med. Biol. 62, 9220.

Geng, C., Moteabbed, M., Seco, J., Gao, Y., Xu, X.G., Ramos-Méndez, J., Faddegon, B., Paganetti, H., 2015. Dose assessment for the fetus considering scattered and secondary radiation from photon and proton therapy when treating a brain tumor of the mother. Phys. Med. Biol. 61, 683.

Gill, T.P., 1965. The Doppler Effect: an Introduction to the Theory of the Effect. Academic Press.

Golnik, C., Hueso-González, F., Müller, A., Dendooven, P., Enghardt, W., Fiedler, F., Kormoll, T., Roemer, K., Petzoldt, J., Wagner, A., 2014. Range assessment in particle therapy based on prompt γ-ray timing measurements. Phys. Med. Biol. 59, 5399.

Gunzert-Marx, K., Iwase, H., Schardt, D., Simon, R., 2008. Secondary beam fragments produced by 200 MeV u− 1 12C ions in water and their dose contributions in carbon ion radiotherapy. New J. Phys. 10, 075003.

He, J.P., Tang, X.B., Gong, P., Wang, P., Wen, L.S., Huang, X., Han, Z.Y., Yan, W., Gao, L., 2018. Rapid radionuclide identification algorithm based on the discrete cosine transform and BP neural network. Ann. Nucl. Energy 112, 1–8.

Huang, Y.-S., Lu, K.-H., 2004. Formulation of the classical and the relativistic Doppler effect by a systematic method. Can. J. Phys. 82, 957–964.

Hueso-González, F., Rabe, M., Ruggieri, T.A., Bortfeld, T., Verburg, J.M., 2018. A full-scale clinical prototype for proton range verification using prompt gamma-ray spectroscopy. Phys. Med. Biol. 63, 185019.

Knopf, A.-C., Lomax, A., 2013. In vivo proton range verification: a review. Phys. Med. Biol. 58, R131.

Kraan, A.C., 2015. Range verification methods in particle therapy: underlying physics and Monte Carlo modeling. Front. Oncol. 5, 150.

Krimmer, J., Dauvergne, D., Létang, J., Testa, É., 2018. Prompt-gamma monitoring in hadrontherapy: a review. Nucl. Instrum. Methods Phys. Res. Sect. A Accel. Spectrom. Detect. Assoc. Equip. 878, 58–73.

Lechner, A., Ivanchenko, V., Knobloch, J., 2010. Validation of recent Geant4 physics models for application in carbon ion therapy. Nucl. Instrum. Methods Phys. Res. Sect. B Beam Interact. Mater. Atoms 268, 2343–2354.

Lin, H.-H., Chang, H.-T., Chao, T.-C., Chuang, K.-S., 2017a. A comparison of two prompt gamma imaging techniques with collimator-based cameras for range verification in proton therapy. Radiat. Phys. Chem. 137, 144–150.

Lin, Y.-S., Chao, T.-C., Hong, J.-H., Tung, C.-J., 2017b. Comparisons of longitudinal and lateral dose profiles and relative biological effectiveness for DNA double strand breaks among 1H, 4He and 12C beams. Radiat. Phys. Chem. 137, 169–172.

Liu, H., Zhou, M., Zhang, Z., Shu, J., Liu, T., Zhang, T., 2015. Multi-order blind deconvolution algorithm with adaptive Tikhonov regularization for infrared spectroscopic data. Infrared Phys. Technol. 71, 63–69.

Loeffler, J.S., Durante, M., 2013. Charged particle therapy—optimization, challenges and future directions. Nat. Rev. Clin. Oncol. 10, 411.

Min, C.H., Lee, H.R., Kim, C.H., Lee, S.B., 2012. Development of array-type prompt gamma measurement system for in vivo range verification in proton therapy. Med. Phys. 39, 2100–2107.

Min, C.H., Zhu, X., Winey, B.A., Grogg, K., Testa, M., El Fakhri, G., Bortfeld, T.R., Paganetti, H., Shih, H.A., 2013. Clinical application of in-room positron emission tomography for in vivo treatment monitoring in proton radiation therapy. Int. J. Radiat. Oncol. Biol. Phys. 86, 183–189.

Moteabbed, M., España, S., Paganetti, H., 2011. Monte Carlo patient study on the comparison of prompt gamma and PET imaging for range verification in proton therapy. Phys. Med. Biol. 56, 1063.

Ortega, P., Torres-Espallardo, I., Cerutti, F., Ferrari, A., Gillam, J., Lacasta, C., Llosá, G., Oliver, J., Sala, P., Solevi, P., 2015. Noise evaluation of Compton camera imaging for proton therapy. Phys. Med. Biol. 60, 1845.

Paganetti, H., 2012. Range uncertainties in proton therapy and the role of Monte Carlo simulations. Phys. Med. Biol. 57, R99.

Perl, J., Shin, J., Schümann, J., Faddegon, B., Paganetti, H., 2012. TOPAS: an innovative proton Monte Carlo platform for research and clinical applications. Med. Phys. 39, 6818–6837.

Priegnitz, M., Helmbrecht, S., Janssens, G., Perali, I., Smeets, J., Vander Stappen, F., Sterpin, E., Fiedler, F., 2015. Measurement of prompt gamma profiles in inhomogeneous targets with a knife-edge slit camera during proton irradiation. Phys. Med. Biol. 60, 4849.

Resnick, R., 1971. Introduction to Special Relativity.

Schaffner, B., Pedroni, E., 1998. The precision of proton range calculations in proton radiotherapy treatment planning: experimental verification of the relation between CT-HU and proton stopping power. Phys. Med. Biol. 43, 1579.

Schneider, U., Pedroni, E., Lomax, A., 1996. The calibration of CT Hounsfield units for radiotherapy treatment planning. Phys. Med. Biol. 41, 111.

Schulz-Ertner, D., Jaekel, O., Schlegel, W., 2006. Radiation therapy with charged particles. Semin. Radiat. Oncol. 16, 249–259.

Traini, G., Battistoni, G., Bollella, A., Collamati, F., De Lucia, E., Faccini, R., Ferroni, F., Frallicciardi, P.M., Mancini-Terracciano, C., Marafini, M., 2017. Design of a new tracking device for on-line beam range monitor in carbon therapy. Phys. Med. 34,

18–27.

Tsujii, H., Kamada, T., 2012. A review of update clinical results of carbon ion radio-therapy. Jpn. J. Clin. Oncol. 42, 670–685.

Tsujii, H., Kamada, T., Shirai, T., Noda, K., Tsuji, H., Karasawa, K., 2014. Carbon-ion Radiotherapy. Carbon-Ion Radiotherapy. Springer.

Verburg, J.M., Riley, K., Bortfeld, T., Seco, J., 2013. Energy-and time-resolved detection of prompt gamma-rays for proton range verification. Phys. Med. Biol. 58, L37.

Verburg, J.M., Seco, J., 2014. Proton range verification through prompt gamma-ray

spectroscopy. Phys. Med. Biol. 59, 7089.

Verburg, J.M., Shih, H.A., Seco, J., 2012. Simulation of prompt gamma-ray emission during proton radiotherapy. Phys. Med. Biol. 57, 5459.

Xie, Y., Bentefour, E.H., Janssens, G., Smeets, J., Vander Stappen, F., Hotoiu, L., Yin, L., Dolney, D., Avery, S., O'Grady, F., 2017. Prompt gamma imaging for in vivo range verification of pencil beam scanning proton therapy. Int. J. Radiat. Oncol. Biol. Phys. 99, 210–218.